POLITECNICO DI TORINO
Repository ISTITUZIONALE

Effect of heat treatment on microstructure and oxidation properties of Inconel 625 processed by LPBF

Original
Effect of heat treatment on microstructure and oxidation properties of Inconel 625 processed by LPBF / Parizia, S.; Marchese, G.; Rashidi, M.; Lorusso, M.; Hryha, E.; Manfredi, D.; Biamino, S.. - In: JOURNAL OF ALLOYS AND COMPOUNDS. - ISSN 0925-8388. - ELETTRONICO. - 846:(2020), p. 156418. [10.1016/j.jallcom.2020.156418]

Availability:
This version is available at: 11583/2844274 since: 2020-09-07T17:10:48Z

Publisher:
Elsevier Ltd

Published
DOI:10.1016/j.jallcom.2020.156418

Terms of use:

This article is made available under terms and conditions as specified in the corresponding bibliographic description in the repository

Publisher copyright

(Article begins on next page)

07 May 2026

Effect of heat treatment on microstructure and oxidation properties of Inconel 625 processed by LPBF

Simone Parizia[1,2*], Giulio Marchese[1], Masoud Rashidi[3,4], Massimo Lorusso[2], Eduard Hryha[3], Diego Manfredi[1], and Sara Biamino[1]

[1]*Department of Applied Science and Technology, Politecnico di Torino, Corso Duca degli Abruzzi 24, 10129 Torino, Italy.*

[2]*Center for Sustainable Future Technologies - CSFT@PoliTo, Istituto Italiano di Tecnologia, Via Livorno 60, 10144 Torino, Italy*

[3]*Department of Industrial and Materials Science, Chalmers University of Technology, 41296 Göteborg, Sweden*

[4]*School of Mechanical and Aerospace Engineering, Nanyang Technological University, 50 Nanyang Ave, Singapore, 639798, Singapore*

*Corresponding author: simone.parizia@polito.it Tel +390110904763

Abstract

This paper presents a study of the microstructure evolution due to oxidation exposure of Inconel 625 (IN625) alloy produced by Laser Powder Bed Fusion (LPBF). IN625 is a nickel-based superalloy characterized by good mechanical properties, excellent oxidation, and corrosion resistance from cryogenic temperatures up to 980 °C, allowing its wide use in various harsh environments. In order to enable the application of LPBF IN625 components at high temperatures, the oxidation properties and microstructure of as-built and post-heat treated LPBF IN625 alloy must be carefully investigated. For this reason, an extensive characterization of the oxidation behavior of the alloy in the as-built condition and after solution treatment was performed. For both these conditions, the oxidation treatments were performed at 900 °C up to 96 h. The characterization was performed using scanning electron microscopy (SEM), energy-dispersive X-ray spectroscopy (EDS), X-ray diffraction (XRD), and scratch test analysis. The characteristics of the oxide layer and formed phases were investigated. The as-built IN625 state presented greater oxidation resistance compared to the solutionized IN625 one. The latter condition showed a defected oxide layer with the presence of Nb and Ni oxides inside the Cr oxide layer.

Keywords: Laser powder bed fusion, Additive manufacturing, Nickel-based superalloys, Inconel 625, oxidation, microstructure evolution.

1.0 Introduction

Nickel-based superalloys are widely applied in sectors such as aerospace, aeronautic, nuclear, marine, chemical, and petrochemical [1,2]. Their wide application is mainly due to the excellent resistance in harsh environments, preserving high mechanical and oxidation properties. They exhibit very high oxidation resistance at high temperatures, resulting in lower mechanical properties degradation in comparison with other materials such as stainless steel and titanium alloys [3,4]. However, their elevated mechanical properties at high temperatures make it difficult to process this class of alloys, increasing the machining costs [5,6]. Additive Manufacturing (AM) processes can be attractive for overcoming the issues related to materials with low machinability. Among the AM technologies, Laser Powder Bed Fusion (LPBF) has been widely used for the fabrication of these alloys [7–12]. This process allows the production of dense parts, layer by layer, starting from a layer of powder selectively

melted by a laser beam, leading to improved design freedom compared to traditional forming technologies [12,13].

Inconel 625 alloy is one of the most processed LPBF Nickel-based alloys, which is characterized by high-temperature strength coupled with outstanding corrosion and oxidation resistance [7,14–16]. A considerable amount of literature has been published on the oxidation resistance of traditional produced IN625 alloy under different conditions, such as in the presence of steam, supercritical water, and air [17–21].

However, it is crucial to consider that the very high cooling rates of the LPBF process (up to 10^7 K/s [22]), leads to a non-equilibrium microstructure with fine dendritic/cellular structures having dimensions typically inferior to 1 µm. Moreover, the microstructure of the LPBF IN625 is characterized by anisotropy with elongated grains parallel to the building direction [7,12,23]. It is therefore evident that LPBF IN625 alloy under service at high temperatures can be subjected to a different microstructure evolution compared to the same alloy produced by traditional technologies, influencing its oxidation resistance. In particular, the IN625 alloy is subjected to the formation of several phases under thermal exposures such as the metastable **γ''** (Ni_3Nb, body-centered tetragonal ordered) and its stable form **δ** (Ni_3Nb, orthorhombic) [24], as well as the formation of different types of carbides ($M_{23}C_6$, M_6C, and MC) [25–27].

For IN625, one of the suggested heat treatment is the solution annealing treatment at 1150 °C 2 h. This heat treatment removes segregations, secondary phases, active recrystallization, and grain growth [7,14,28–31].

In literature, the majority of the studies on LPBF IN625 alloy investigated the effect of the process parameters and heat treatments on the microstructure and mechanical properties. To the authors' knowledge, only a few studies evaluated the corrosion resistance [32,33] and the oxidation properties for the LPBF IN625 alloy [34,35].

IN625 is mostly used for its high corrosion and oxidation resistance in a temperature range between cryogenic and 980°C [28], for applications in aircraft ducting systems, engine exhaust systems [36], turbine shroud rings, and heat-exchanger tubing in systems such as the solar-hybrid gas-turbine [28,37]. Moreover, it is one of the few alloys allowed by the ASME Boiler and Pressure Vessel Code to operate in pressure vessels up to 980 °C [36]. It is, therefore, crucial to evaluate the oxidation properties of the LPBF produced alloy, identifying possible microstructure modification under heat treatments.

In this study, the oxidation resistance of the as-built and solution annealed (1150 °C 2h) IN625 states under thermal exposure at 900°C was evaluated. The temperature was selected to study the first oxidation regime, identified through thermal gravimetric analysis (TGA). The current study provides an in-depth investigation of the as-built and post-heat treated IN625 conditions on their different microstructure development and oxidation phenomenon. The formed oxides were analyzed by scanning electron microscopy (SEM) imaging, X-ray diffraction (XRD) analysis, and scratch tests.

2.0 Materials and methods

The IN625 powder used for this work was purchased from EOS GmbH, with a declared chemical composition (wt.%) as reported in Table 1, which is under the UNS N06625. The powder size distribution was characterized by a d10 of 16 µm and d90 of 48 µm using laser granulometry.

Table 1: IN625 declared composition in weight percentage (wt %)

Ni	Cr	Mo	Nb	Fe	Ti, Al	Co	C	Ta	Si, Mn	P, S
≥58	20-23	8-10	3.15-4.15	≤5	≤0.4	≤1	≤0.1	≤0.05	≤0.5	≤0.015

An EOSINT M270 Dual Mode (EOS GmbH) machine, equipped with a 200 W Yb fibre laser with a spot size of 100 µm, was used. Samples with dimensions of 8x20x30 mm^3 were produced using the following parameters: laser power of 195 W, scan speed of 1200 mm/s, hatching distance of 0.09 mm, and a layer thickness of 20 µm. The scanning strategy consisted of a 67° laser beam scanning rotation between consecutive layers, as suggested by EOS. Previous work proved that these parameters resulted in IN625 specimens with high relative density (≥99.97%) [16]. After removing the samples from the building platform, a solution treatment was performed on a group of samples, for 2 h at 1150 °C in air, followed by water quenching. This is the suggested solution treatment for this superalloy [29].

From now on, the as-built and solutionized samples will be abbreviated as AB and SOL, respectively. All the samples were carefully polished using 1200 SiC grind papers, paying attention to preserve the geometry. In the case of SOL samples, the polishing was performed after the solution treatment, in order to completely remove the roughness but also the oxides formed during the solution treatment itself. After polishing, the specimens were weighed on a precision balance (sensibility of 0.1 mg) and the volumes were determined using a caliber (sensibility of 0.1 mm).

For the AB and SOL conditions, the oxidation treatments were conducted at 900 °C for 8, 24, 48, 72, and 96 h. In order to evaluate the variations in mass, for each selected time, the oxidized samples were removed from the furnace, air-cooled, and then weighted. The uncertainty of the mass gain was calculated through the propagation of error, considering the sensibility of the caliber and precision balance. Afterward, each sample was cut considering the orientations schematically reported in Fig. 1. Notice that the axes are oriented as the sample was oriented during the production process (Z-axis is parallel to the building direction while X is parallel to the powder distribution in the layers). Finally, the samples were cleaned in an ultrasonic bath in ethanol and then in acetone, in order to remove dirt and polishing residuals.

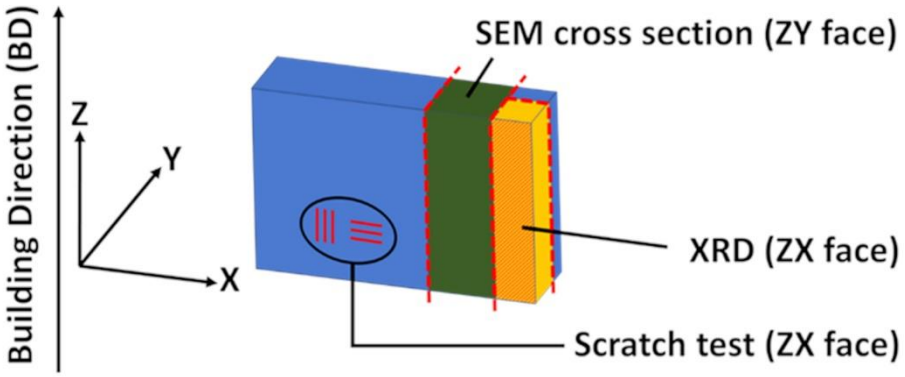

Figure 1: schematically illustration of the samples preparation

2.1 TGA (Thermal Gravimetric Analysis)

The mass gain of IN625 in the AB and SOL states in the temperature range from 25 up to 1200°C has been evaluated using a Mettler Toledo 1600 TGA system. The heating rate has been settled at 10°C/min, with an air flux of 50 ml/s.

2.2 Cross-sections analysis

Cross-section samples were mounted in conductive mounting resin and polished with grinding papers and diamond pastes up to 1 µm, and then polished with OP-S colloidal silica (0.04 µm). The polished samples were

analyzed by means of SEM (Phenom XL, Phenom-World BV) and a field emission gun scanning electron microscope (FEG-SEM, LEO 1550, Zeiss), equipped with an X-ray energy diffraction spectroscopy (EDS) unit (X-MAX, Oxford Instruments). The fraction of phases and layer thicknesses were determined by Image J software. For the characterization of phases, 20 particles were analyzed for each condition, while for the determination of the oxide layer thickness, 10 images were used for each sample, measuring the oxide thickness in 5 points for each image.

In order to make clearly visible the microstructure and precipitates, the cross-sections are shown with high contrast backscattered (BS) SEM images. Moreover, since the high contrast images hide the oxide presence, low contrast SEM images of the same locations are displayed, and a higher magnification of the oxide layer is provided to better observe the oxide features.

2.3 XRD analyses

X-ray diffraction analyses (XRD, PANalytical, Almeno, The Netherland) were conducted using CuKα radiation (wavelength 1,5418E-10 m) in a Bragg Brentano configuration with **θ** range from 15° to 100°, employing a step size of 0.013° and a counting time of 35 s per step. The analysis was performed on both AB and SOL samples before oxidation and after 8 h and 96 h oxidation. For the analysis, the ZX plane, which represents the most extended side of the samples, was selected. Three XRD analyses were performed on each sample. The lattice parameter of the matrix was evaluated using Bragg's law (equation 1).

$$\boldsymbol{n\lambda = d_{h,k,l} \sin\theta} \quad \textbf{(1)}$$

Where **λ** is the wavelength of the radiation used, **d** is the interplanar distance, and **θ** is the angle of the peak considered. Nelson-Riley method [38] was used in order to obtain a good evaluation of the lattice constant, considering 111, 200, 220, 311, and 222 peaks of the **γ** austenitic matrix (the typical peaks used in literature in order to calculate the lattice parameter of Ni-based superalloys). This method used more peaks of the same phase allowing to reduce the errors of the measurement [15,31,38,39].

The lattice parameter is plotted versus a Nelson-Riley coefficient calculated using equation 2:

$$\boldsymbol{Nelson - Riley\ coeff.} = \frac{1}{2}\left(\frac{\cos\theta^2}{\sin\theta} + \frac{\cos\theta^2}{\theta}\right) \quad \textbf{(2)}$$

The lattice parameter was calculated using the linear fitting, considering the value where the Nelson-Riley coefficient value is equal to 0. An example of the employed approach is provided in Fig.2.

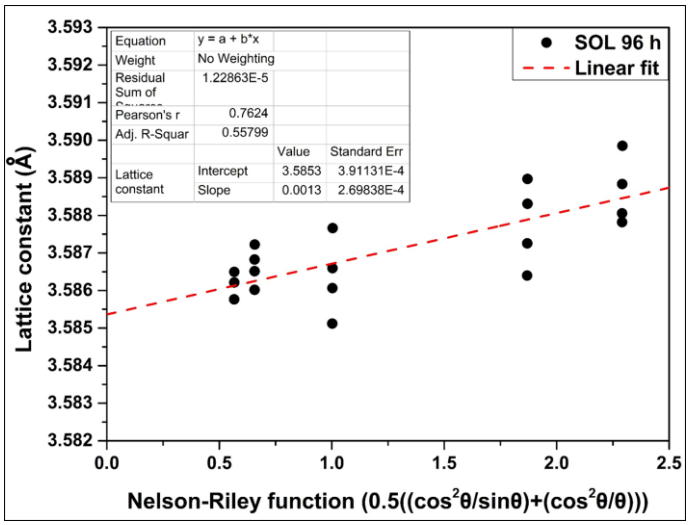

Figure 2: Example of the Nelson-Riley method used to determine the lattice parameter of the austenitic matrix of the alloy

2.4 Scratch tests analysis

The resistance of the oxide layer was evaluated through scratch tests performed with a nano-indenter system (Hysitron TI 950 Triboindenter, Hysitron-Bruker). Each condition (AB and SOL, both after 8 and 96 h of oxidation treatments) was tested with three scratches parallel to the building direction (BD) and three scratches perpendicular to the BD, for highlighting possible variations, as displayed in Fig. 1. The test consisted of a scratch 1 mm long, increasing linearly the normal force applied from 0 mN to 250 mN. During the indentation, the lateral force needed by the indenter for the move is recorded. Finally, the scratches have been observed by means of SEM analysis.

3.0 Results and discussion

3.1 TGA analysis

An explorative TGA in air was performed on both AB and SOL IN625 samples in order to evaluate their oxidation regimes, as reported in Fig. 3. Both conditions showed a constant mass gain rate up to ≈950 °C. Above this temperature, the mass gain rate increased, indicating a different oxidation mechanism (second oxidation regime). The AB sample showed a slightly higher mass gain compared to the SOL specimen. In order to investigate the first oxidation regime, the oxidation temperature of 900 °C was selected.

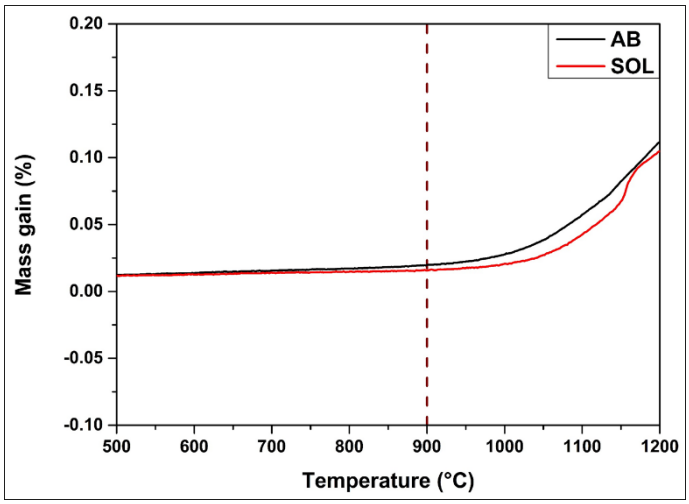

Figure 3: Results of the TGA analysis, reported as mass gain % vs. temperature

3.2 Mass gain evaluation and oxidation thickness

The mass gain over the time of oxidation treatment at 900 °C for the AB and SOL IN625 states is displayed in Figure 4a. Both conditions exhibited a similar mass gain up to 48 h, but they started to diverge for prolonged times. The AB condition slows its mass gain, while the SOL oxidation rate remained mostly unchanged. Considering the assumption that the oxide layer was not porous, with good adhesion, equation (3) can be used in order to evaluate a constant of oxidation ($\mathbf{K_p}$) for the AB and SOL states [40].

$$\left(\frac{\Delta w}{A}\right)^2 = K_p * \mathbf{t} \quad \textbf{(3)}$$

Where **Δw** is the mass gain, **A** (cm^2) is the area of the sample, and **t** (h) is the time [41]. This assumption allows to obtain an apparent $\mathbf{K_p}$ ($mg^2*cm^{-4}*h^{-1}$), useful for comparing the two conditions, as already applied in the literature for IN625 alloy and other superalloys [40,42]. Based on the equation (3), the $\mathbf{K_p}$ of the AB and SOL conditions were assessed as reported in Fig. 4b. Up to 48 h of thermal exposures at 900 °C, the AB revealed $\mathbf{K_p}$ of (14±1)E-4 while it is (15±1)E-4 for the SOL state. Subsequently, from 48 to 96 h, the $\mathbf{K_p}$ of the AB did not change, while it became almost double for the SOL condition (29±1)E-4.

Fig.4c reveals the layer thickness evolution of the AB and SOL conditions correlated with the oxidation treatment at 900 °C experimentally evaluated. The layer thickness of the oxide AB and SOL samples presented similar dimensions up to 48 h, and then, the SOL condition showed a considerable increment of the oxide thickness for prolonged thermal exposure. Additionally, for the SOL state, the high standard deviation derived from the less uniform formation of the oxide layer compared to the one in the AB state.

The kinetic deviation between the two conditions starting from 48 h was caused by the formation of defects in the SOL oxide layer. This resulted in the spallation of the oxides (see Figure 5e and 5f, red arrows). Moreover, the absence of a compact layer of oxide (cracks indicated by the grey dashed arrows in fig. 5e and 5f) did not protect the matrix, leading to an inferior oxidation resistance correlated with an increment of oxidation kinetics, in comparison with the AB state. The different mechanisms generating the deviation of the oxidation kinetic will be studied in the following paragraphs. For this reason, the early stage of the oxidation (AB and SOL states after oxidation for 8 h) and the final part (AB and SOL after oxidation for 96 h) will be deeply analyzed. The first one was chosen to investigate the types of oxides and the microstructure of the samples under initial oxidation

treatments. In contrast, the second one was chosen with the aim to determine the microstructural features and oxidation properties during prolonged oxidation exposures for the two conditions.

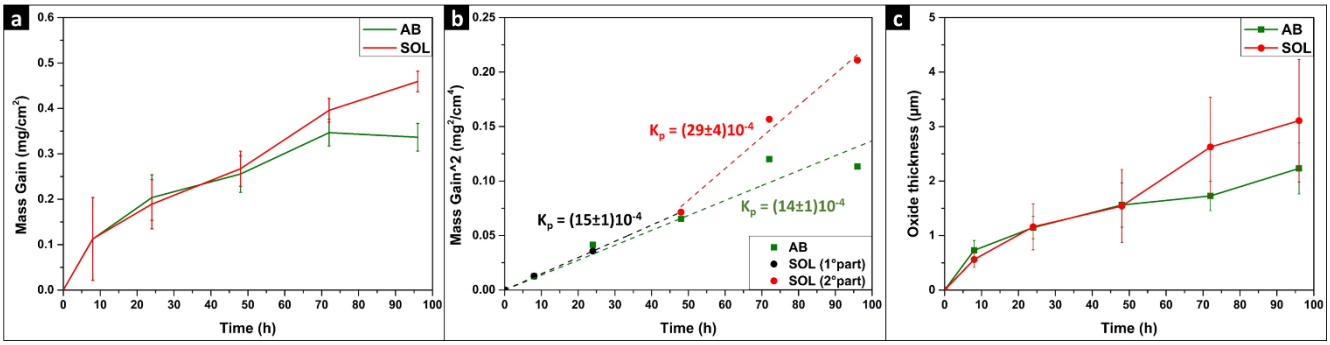

Figure 4: mass gain (a), square mass gain (b) and oxide layer thickness (c) evolution increasing oxidation time

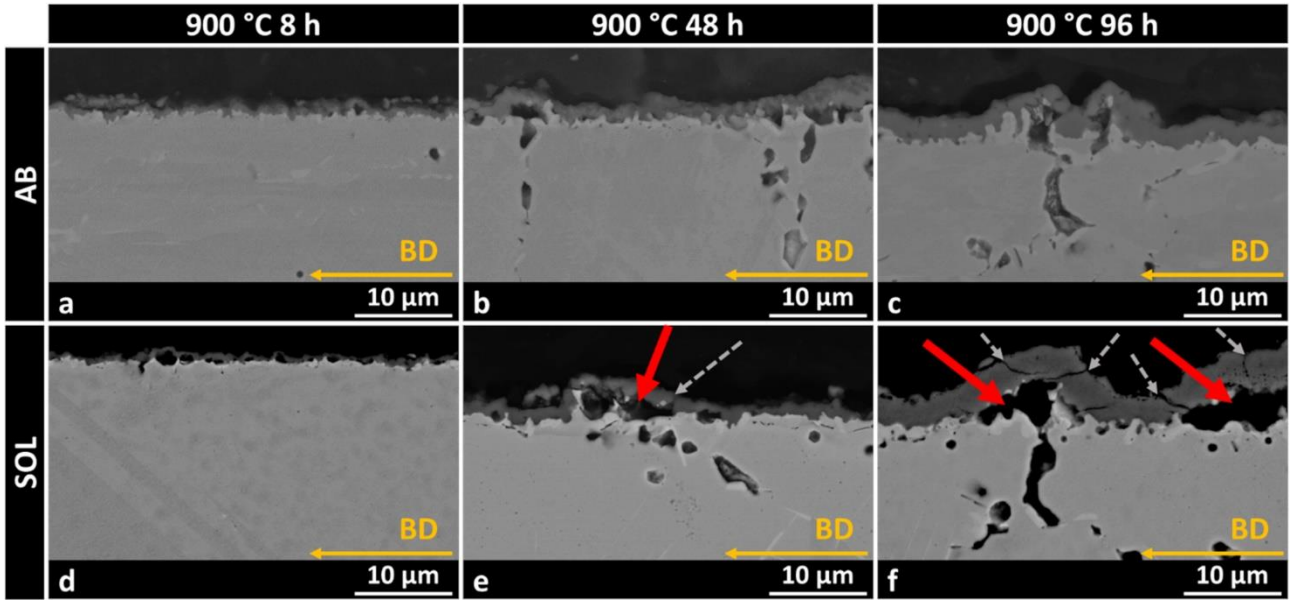

Figure 5: cross-section of the oxide layer for the IN625 AB oxidized for (a) 8 h, (b) 48 h, (c) 96 h, and for the IN625 SOL oxidized for (d) 8 h, (e) 48 h, and (f) 96 h

3.3 Microstructural analysis of the cross-sections

3.3.1 AB LPBF IN625 oxidized for 8 h

For the AB IN625 after 8 h of thermal exposure, the oxide layer (Fig.6a and 6c) is mainly compact and continuous. The alloy below presents bright precipitates primarily located at the grain boundaries (GBs) (thick red arrows, Fig.6a, 6b, 6c, 8), as well as precipitates inside the grains (red rounded, Fig.6b) and at the alloy/ oxide layer interface (thin dashed yellow arrows, Fig.6a, 6b, 6c and 8).

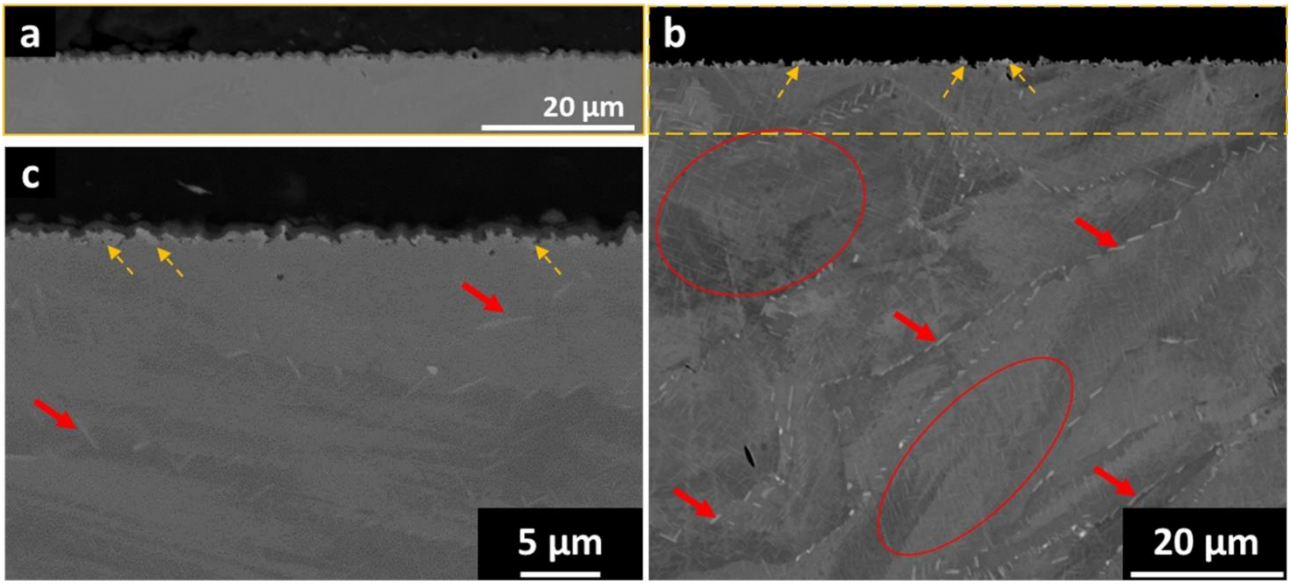

Figure 6: High contrast (a) and low contrast (b) BS SEM image of the cross-section, high magnification image of the cross-section (c) of AB IN625 oxidized for 8 h

Analyzing the XRD pattern of the oxidized surface (Fig. 7), it consisted of Cr_2O_3, the typical oxide for the IN625 [19], including a minor presence of TiO_2. The other peaks reported in the XRD pattern are characteristic of the FCC matrix (**γ**) and the **δ** phase.

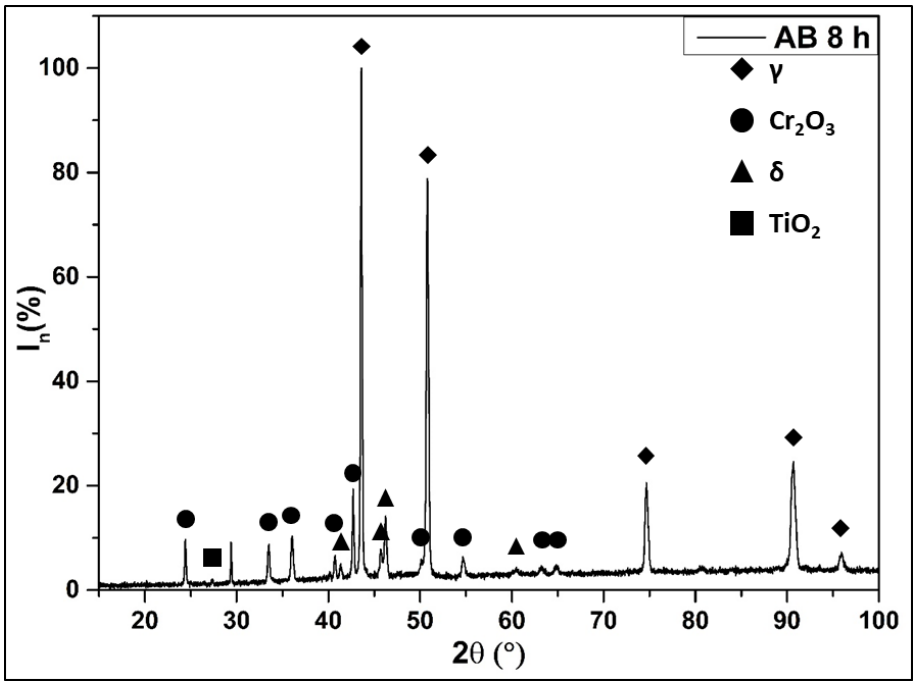

Figure 7: XRD of the oxidized ZX surface of AB IN625 oxidized for 8 h

In accordance with the XRD analysis, EDS maps (Fig.8) highlighted the Cr and Ti enrichment in the oxide layer. Moreover, the EDS maps pointed out Cr depletion at the alloy/oxide interface, coupled with Nb enrichment. The Cr depletion is chiefly due to the migration in the oxide, and this depletion triggers the Nb migration because the Nb solubility in Ni alloy is higher for lower Cr concentration. This phenomenon is also reported from other researchers in literature [43,44].

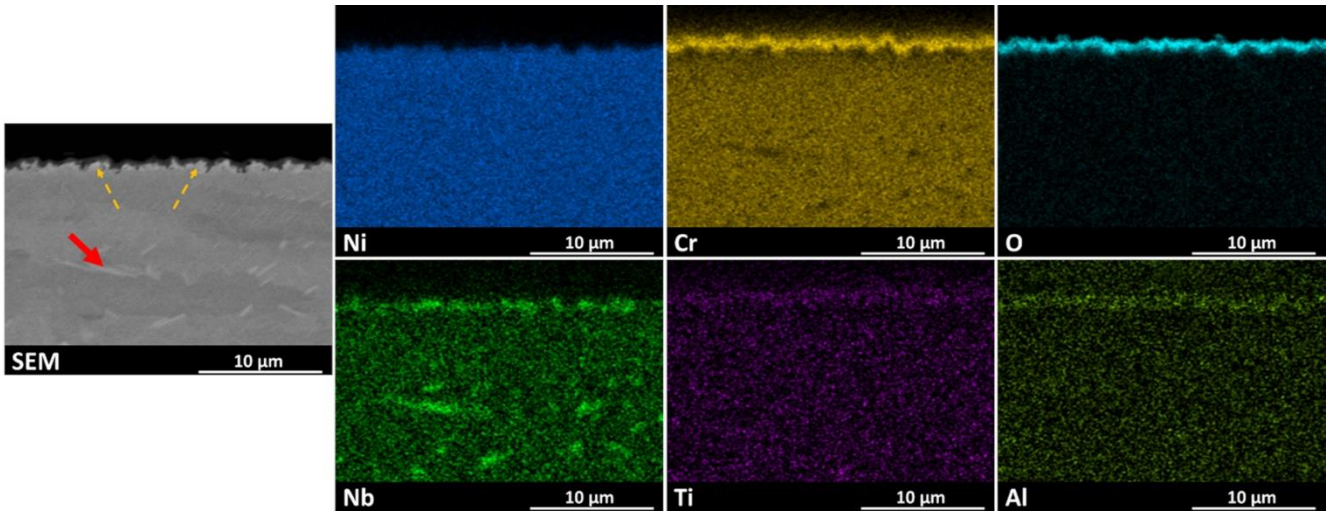

Figure 8: EDS maps of the cross-section of AB IN625 oxidized for 8 h

The microstructure is characterized by columnar grains elongated along the building direction, which is common in IN625 processed by LPBF [7,16,27,45]. The thermal exposure involved the formation of **δ**-phases (bright precipitates in SEM images), located both inside the grains and along the GBs. GB precipitates (Fig.6b and 6c, thick red arrows) are generally bigger compared to the ones inside the grains (Fig.6b, red rounded). The majority of **δ**-phases (Ni_3Nb) at the GBs reached a length of around 3 µm, even though larger **δ**-phase precipitates can be detected. They tend to form along <111> direction and at the GBs as confirmed in literature [45,46]. The formation of **δ**-phases is also detectable by the XRD pattern (Fig.7), as well as from the Nb enrichment visible in EDS maps in Fig.8 (thick red arrows). Moreover, in the Nb enriched zone under the oxide layer, it is possible to see some precipitate (Fig. 6b, 6c, and Fig.8, thin dashed yellow arrows).

3.3.2 SOL LPBF IN625 oxidized for 8 h

Under thermal exposures for 8 h, the SOL IN625 samples exhibited oxide layer with some holes, located under the oxide layer, as pointed out by thick dashed green arrows in Fig.9a, 9b, and 9c, as well as between the oxide and the matrix, as highlighted by the thin grey arrows in Fig.9a, 9c, and 11. It is interesting to notice the presence of some internal oxidation near to the alloy/oxide layer interface (thick dashed green arrows in Fig.9a, 9b, 9c). The microstructure lost the columnar grain structure after solutionizing treatment, and, in this case, large bright precipitates are present only at the GBs (thick red arrows, Fig.9b) and at the oxide layer/alloy interface (thin dashed yellow arrows, Fig.9b, 9c).

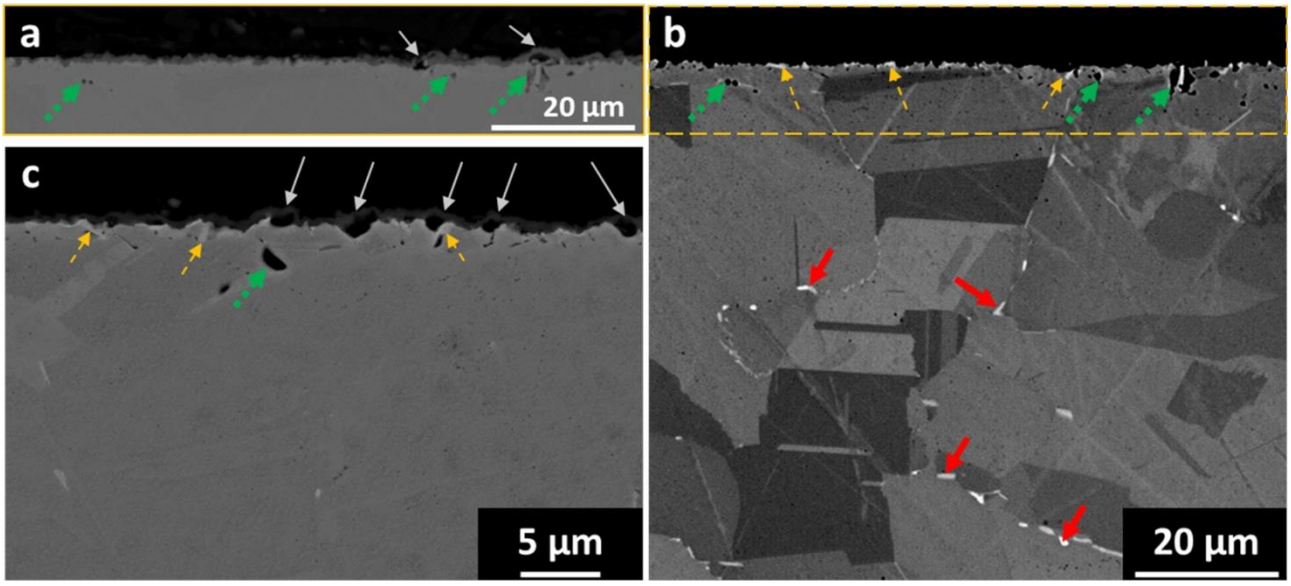

Figure 9: High contrast (a) and low contrast (b) BS SEM image of the cross-section, high magnification image of the cross-section (c) of SOL IN625 oxidized for 8 h

Compared with the AB state subjected to the same thermal exposure, the XRD pattern (Fig.10) revealed that the oxide is composed of Cr_2O_3. On the other hand, TiO_2 peaks were absent, even if Ti can be found from the EDS map (Fig.11). In fact, the concentration of TiO_2 could be under the threshold of the XRD analysis. The reason for this lower Ti content in the oxide layer can be explained with the differences in the elemental distribution inside the matrix between AB and SOL alloy. The segregations present in the AB state are enriched by Nb, Mo, and Ti, and, as a result, the mobility of those elements is modified [47].

Also for the SOL IN625 oxidized for 8 h, it is possible to find Cr depletion coupled with Nb enrichment in the alloy/oxide interface by means of EDS analysis (Fig.11).

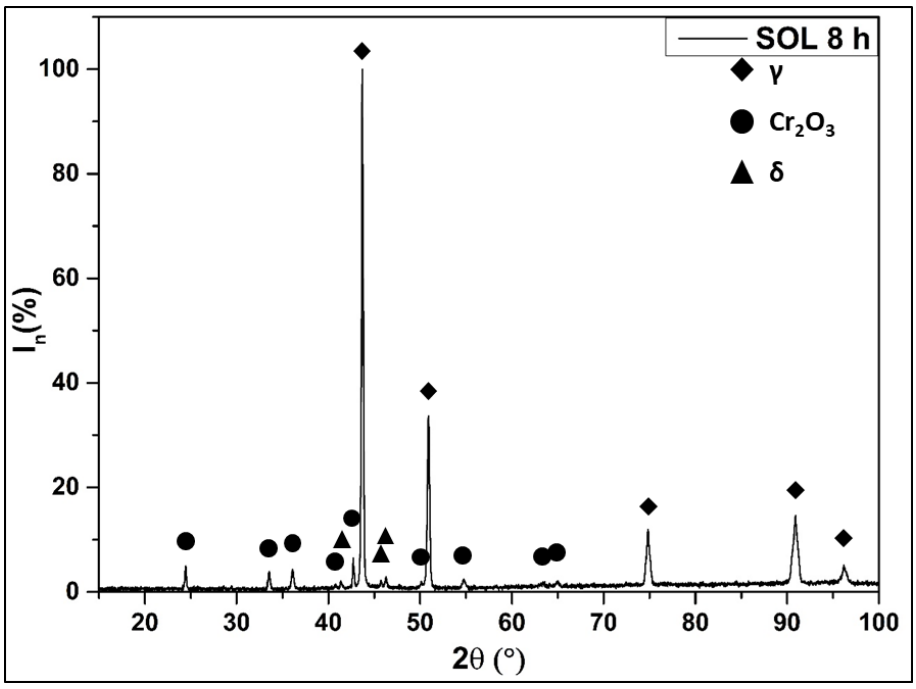

Figure 10: XRD of the oxidized surface of SOL IN625 oxidized for 8 h

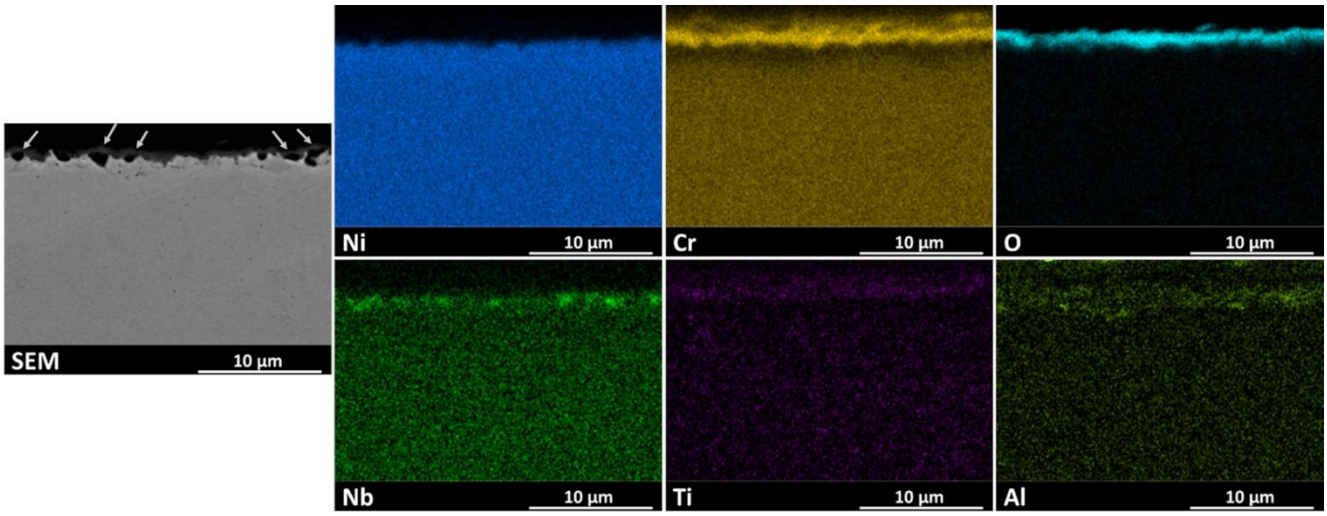

Figure 11: EDS maps of the cross-section of SOL IN625 oxidized for 8 h

Compared to the AB condition, the SOL state present equiaxed grains, with evident twinning GBs [7,30,31]. Figure 9b displayed the formation of **δ**-phases (Fig.9b, thick red arrows), sized around 0.5-3 µm, as observed by the XRD (Fig.10). Also, for this condition, some Nb-rich precipitates are present right under the oxide layer (Fig.9a and 9c, thin dashed yellow arrows).

3.3.3 AB LPBF IN625 oxidized for 96 h

For the AB IN625 after 96 h of thermal exposures, the sample shows a compact and continuous layer (Fig.12a, 12c), without large defects. Additionally, it is also possible to observe intergranular oxidation (thick dashed green arrows in Fig. 12a, 12b, 12c, 14), covering the GBs for an extension up to around 20 µm.

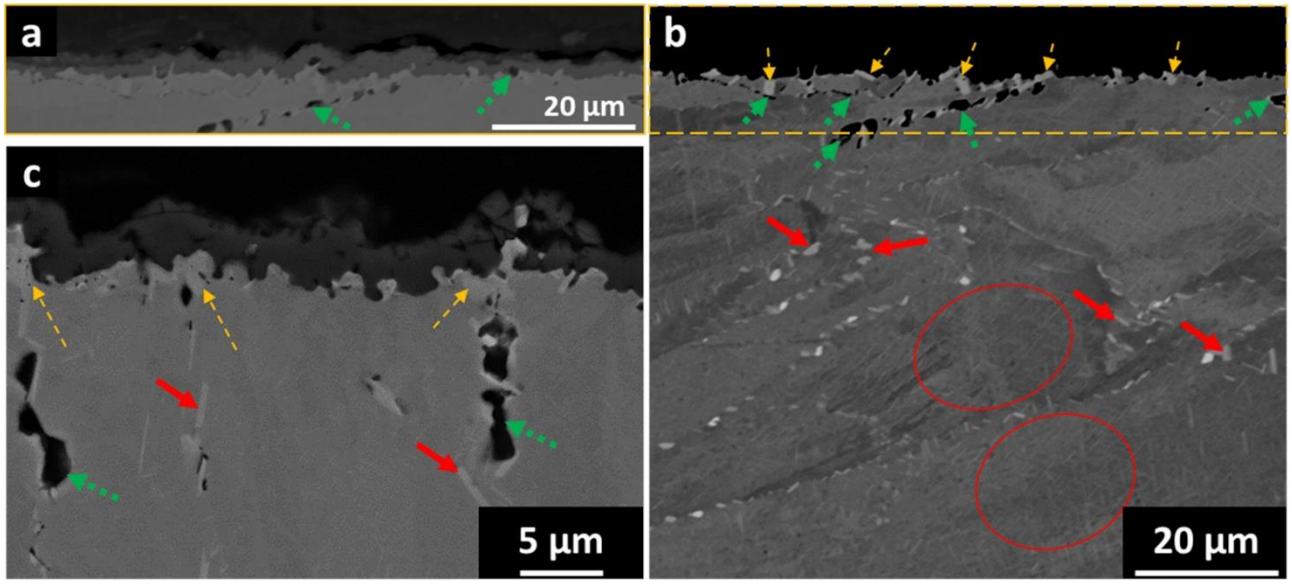

Figure 12: High contrast (a) and low contrast (b) BS SEM image of the cross-section, high magnification image of the cross-section (c) of AB IN625 oxidized for 96 h

XRD pattern (Fig.13) reports the peaks of Cr_2O_3 and TiO_2, indicating the same oxide composition of the AB samples heat-treated for 8 h.

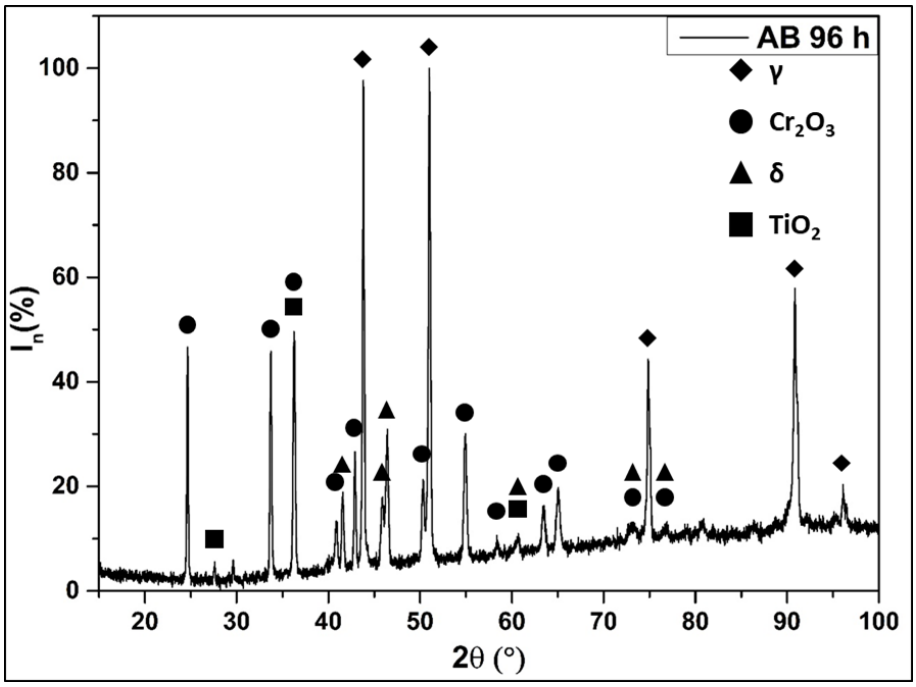

Figure 13: XRD of the oxidized surface of AB IN625 oxidized for 96 h

EDS maps (Fig.14) revealed the presence of Ti and Al in those internal oxides, in accordance with the literature [34,44]. The internal oxides are formed by chemical elements with high oxygen affinity in the cavities formed after the Cr migration in the external oxide layer [34]. According to the Ellingham diagram, the Al is the element that creates the most stable oxide, but the concentration of Al is very low (<0.4 % wt.). The Al tends to be trapped in the cavities formed by the Cr migration, leading to reduced availability of the Al in the external oxide (mainly composed by Cr_2O_3, since the alloy Cr content is around 23 % wt.).

Additionally, Nb is also detected in those locations due to the presence of precipitates at the GBs. It is interesting to notice that there is a presence of thick precipitates at the interface between alloy and oxide (thin yellow arrows in Fig. 12b, 12c), as pointed out by the Nb in the EDS map (Fig.14), and there is a lack of precipitates in the underling 10 µm (Fig.12b).

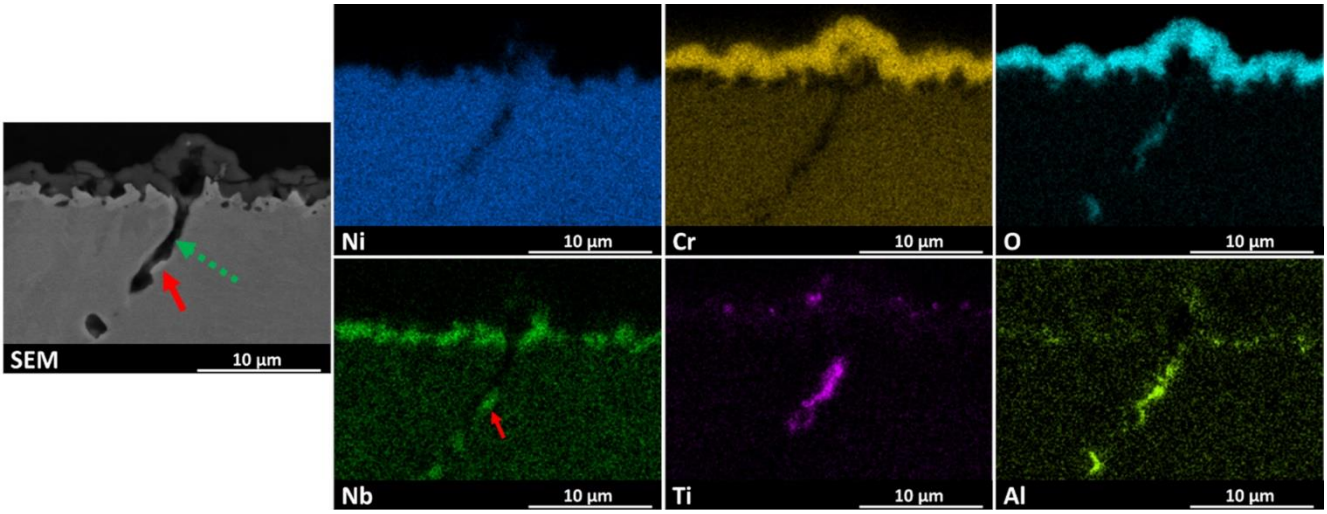

Figure 14: EDS maps of the cross-section of AB IN625 oxidized for 96 h

After thermal exposure for 96 h, the microstructure (Fig.12b) still present columnar grains with **δ**-phases exhibiting the largest precipitates along the GBs (Fig.12b and 12c, thick red arrows) and smaller inside the grains (Fig.12b, red circled). These intergranular revealed the same length compared to the AB condition heat-treated for 8 h. However, for this condition, the quantity of **δ**-phase is higher compared to the AB samples heat-treated for 8 h.

3.3.4 SOL LPBF IN625 oxidized for 96 h

After oxidation treatment for 96 h, the SOL state exhibited cracks within its oxide layer and at the interface between the oxide and the alloy (Fig.15a, 15c, and Fig.17, thin grey arrows), reducing the passivation effect of the oxide layer. The intergranular oxidation penetrated inside the alloy up to around 25 µm following the GBs path (thick dashed green arrows in Fig.15a, 15b, 15c, and Fig.17).

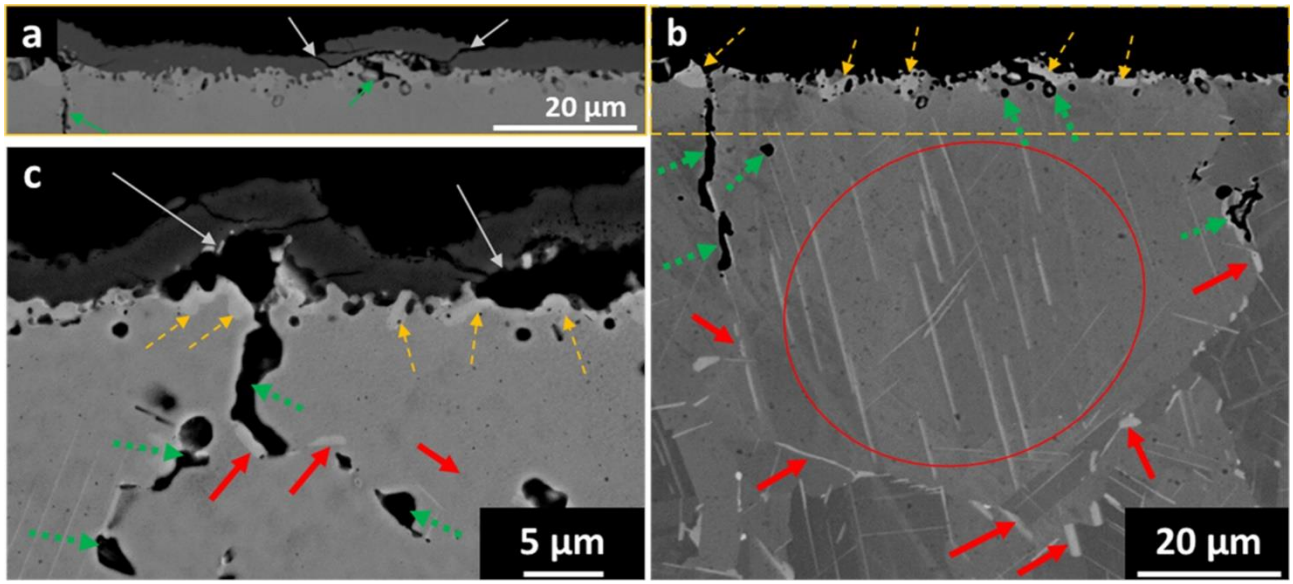

Figure 15: High contrast (a) and low contrast (b) BS SEM image of the cross-section, high magnification image of the cross-section (c) of SOL IN625 oxidized for 96 h

From the XRD pattern (Fig.16), it was possible to determine the presence of Cr_2O_3, and Nb_2O_5 and $NiCr_2O_4$. TiO_2 was not detected by XRD analysis (even if Ti was found in the oxide from the EDS map), because it may be lower the minimum amount detectable.

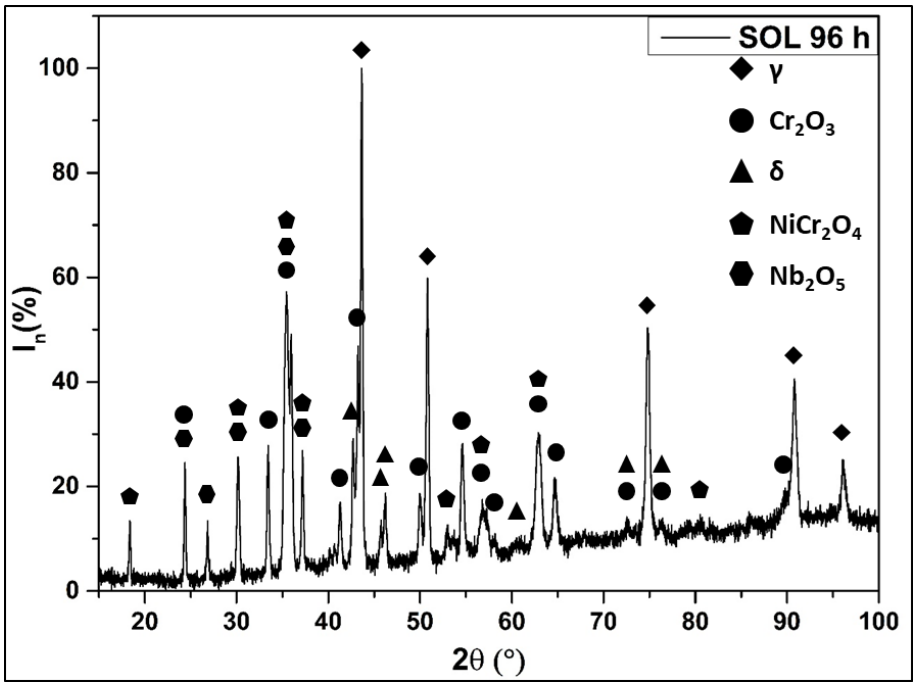

Figure 16: XRD of the oxidized surface of SOL IN625 oxidized for 96 h

In the EDS maps (Fig.17) it can be observed the site of the specimen where the oxide is detached. The detached oxide layer is rich in Cr, O, and Ti in the alloy underlying a new thin oxide layer starts to form, visible in the EDS maps (thick dashed green arrow in the SEM image in Fig.17).

The oxide, characteristic for internal oxidation, in this case, is rich in Ti and Al, similarly to what was observed for the AB samples that underwent 96 h of thermal exposure. Al is also present in the lower part of the detached oxide (Fig. 17), probably incorporated by the oxide when it reached the internal holes (thick dashed green arrows in Fig.15b) near to the oxide.

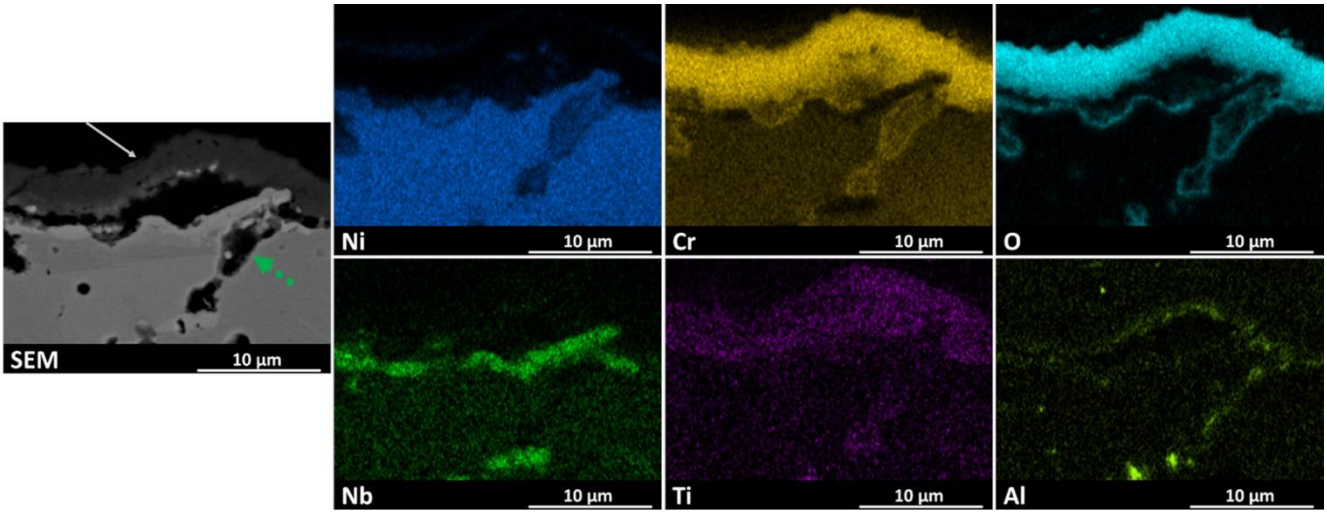

Figure 17: EDS maps of the cross-section of SOL IN625 oxidized for 96 h

Fig.18a shows that in the oxide layer, where it is still well adherent to the alloy, bright clusters surrounded by Cr_2O_3 oxide (red circled) can be found. The EDS maps (Fig.18b) revealed the presence of Ni and Nb in those clusters, confirming the peaks of Nb_2O_5 and $NiCr_2O_4$ revealed by XRD. Those mixed oxides were not uniformly

distributed in the oxide layer, but they could be found only in some locations. It is important to note that no cracks or ruptures are found in the oxide layer close to these mixed oxides, suggesting that they were not related to the poor adhesion or homogeneity of the oxide layer in the SOL state in comparison to the AB state. The shape of those clusters indicates that they are originated from the alloy oxidation, surrounded by an oxide layer.

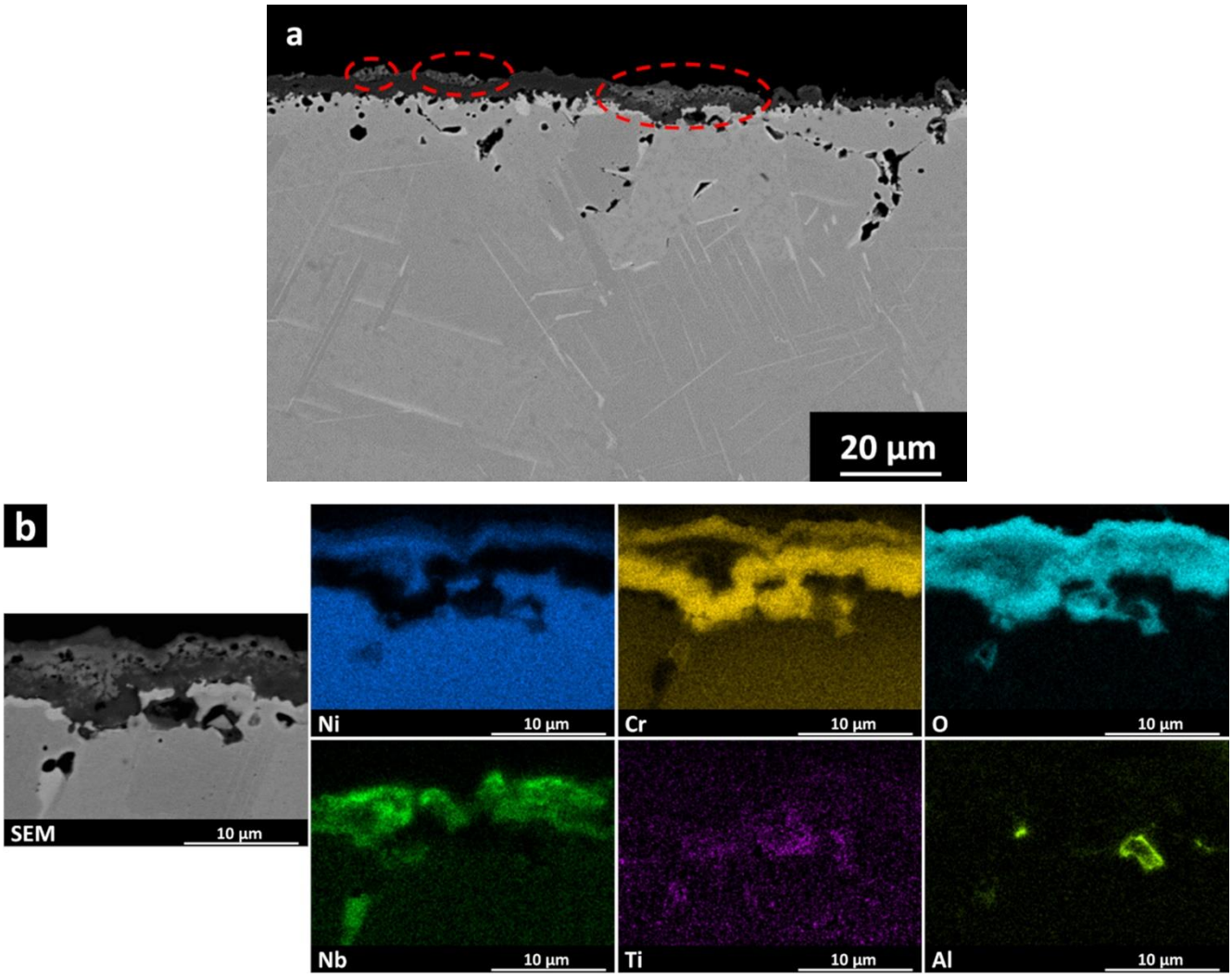

Figure 18: (a) SEM image and (b) EDS map of the mixed oxides in the oxide layer of the 96 h oxidized SOL IN625

A mechanism of such mixed oxide formation is displayed in Fig.19. In Fig.19a, the proposed mechanism of the first oxidation step is presented, where a thin layer of oxide is developed on the alloy surface, with some defects such as spalling and cracks. In the second step, the thermal exposure causes the growth of the oxide layer, which penetrates inside the alloy, including GBs and developing internal oxidation resulting in pores (Fig.19b). Further development of internal oxidation eventually causes the enclosure of some alloy fraction, due to the surrounding GB oxidation. The growing surface oxide layer is further spalled, and the cracks are evolving into spalled oxide rupture (Fig.19c). The volume of the alloy enclosed by oxide possesses lower Cr concentration since it was consumed for the oxide layer formation and hence is enriched in Nb. From this point, the oxidation goes on, developing Nb_2O_5 and $NiCr_2O_4$ oxides, surrounded by the main oxide layer formed by Cr_2O_3 (Fig 19d).

According to the model, the formation of Nb_2O_5 and $NiCr_2O_4$ is caused by the presence of defects in the SOL oxide layer. The defects in the oxide layer locally break the passivation effect, accelerating the oxidation that in some

locations is able to separate part of the alloy from the bulk material. These portions of alloys result separate from the matrix, and therefore the Cr migrations from the matrix cannot reach these areas, involving the formation of Nb_2O_5 and $NiCr_2O_4$ oxides.

After 96 h of thermal exposures, the microstructure of the SOL sample (Fig.15b) shows evident differences compared to the SOL state heat-treated for 8 h (Fig 9b). There was a remarkable **δ**-phases presence inside the grains, reaching length up to around 25 µm (Fig.15b, red circled), as well as in the GB locations (Fig.15b and 15c, red arrows). The growth of the **δ**-phase can be associated with the higher volume concentration of the necessary chemical elements, especially Nb, generated by the dissolution of segregation and interdendritic areas due to the solution annealing treatments. On the other hand, the AB state presents a large concentration of Nb within the interdendritic and GB areas, limiting the availability of Nb, and therefore, drastically reducing the growth of the **δ**-phase. As seen previously in AB 96 h sample (Fig. 12b and 12c), Nb-rich precipitates are formed also in the SOL state at the alloy/oxide interface (thin yellow arrows) and there is a lack of precipitates in the underling 10 µm (Fig.15b). Also, Chyrkin et al. [44] observed Cr_2O_3 layer formation during high-temperature oxidation of IN625, associated with the precipitation of **δ**-phase at the alloy/layer interface and the formation of a precipitate depleted zone in the sub-surface layer.

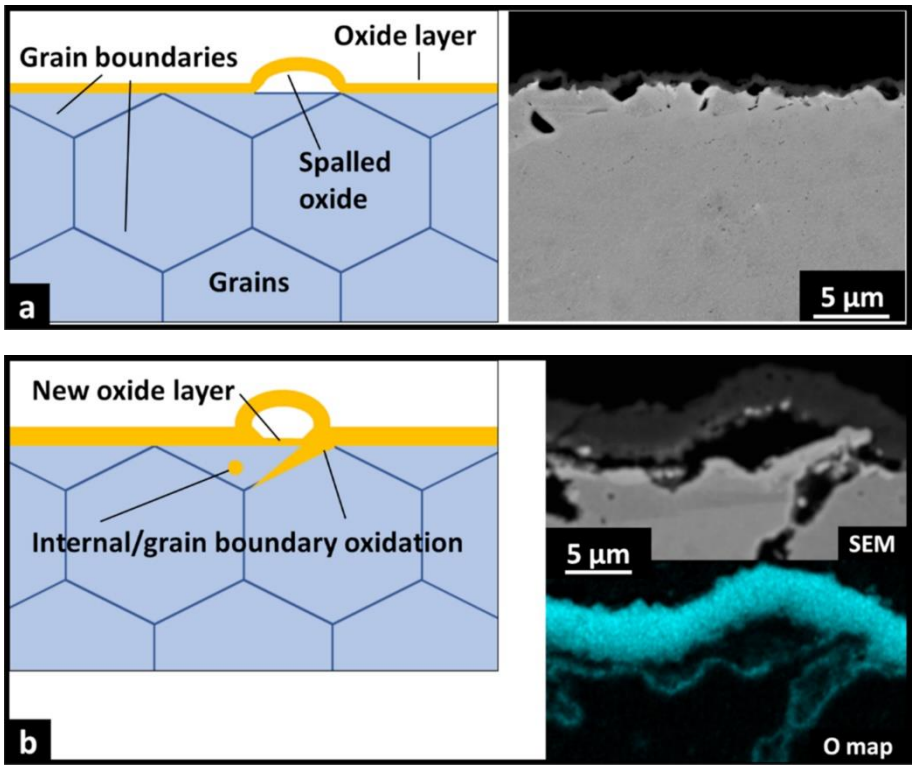

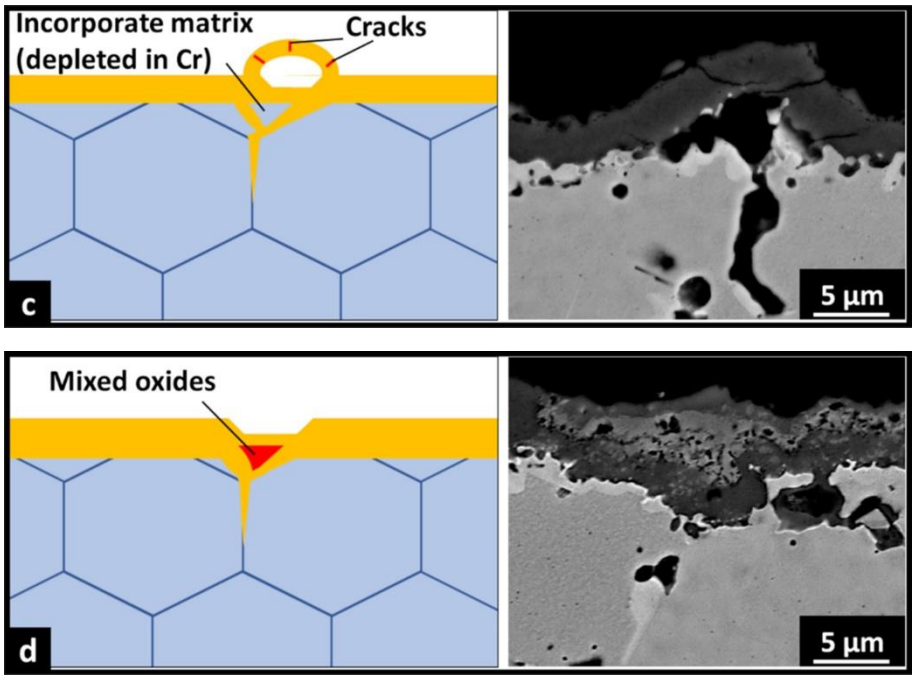

Figure 19: Proposed matrix incorporation mechanism: initial oxidation (a), intergranular and internal oxidation starts (b), alloy surrounded by intergranular oxidation (c) and mixed oxides formation (d)

3.3.5 Summary of phases formation for the different conditions

Table 2 summarizes the phases and oxides formed under the thermal exposures at 900 °C for the AB and SOL conditions.

According to the time-temperature-transformation (TTT) diagram of the conventional IN625 alloy, the formation of **δ**-phase is coherent with a temperature of 900 °C. However, **δ**-phases generation after only 8 h of thermal exposure indicates faster formation due to the presence of Nb-rich segregations [7,48,49]. Moreover, after thermal exposures of 8 h, it is interesting to note that the SOL state presents only intergranular **δ**-phases in contrast to the inter/intragranular **δ** formation in the AB state. This indicates that the solution annealing was effective in eliminating the segregation of the AB material within the grains. After thermal exposure for 96 h, also the SOL state exhibits both intergranular and intragranular **δ**-phases. Note that for all the conditions, a minor presence of carbides could be formed under this temperature. However, their presence is neglectable with respect to the **δ**-phases due to the very low level of carbon [7,31].

Cr_2O_3 and TiO_2 are reported for all the conditions, while the SOL 96 h also revealed Nb_2O_5 and $NiCr_2O_4$ oxides.

Table 2: Detected phases for the heat-treated AB and SOL conditions

	Intergranular δ-phase	Intragranular δ-phase	Cr_2O_3	TiO_2	Nb_2O_5 and $NiCr_2O_4$
AB 8 h	X	X	X	X	
AB 96 h	X	X	X	X	
SOL 8 h	X		X	X	
SOL 96 h	X	X	X	X	X

3.4 XRD analysis

The evolution of the lattice parameter of the austenitic matrix (**γ**-phase) of the alloy under thermal exposures is provided in Figure 20. The SOL state is characterized by a larger lattice parameter compared to AB state in the initial state, due to the chemical homogenization involved in the solution annealing, followed by the quenching that freezes the formation of secondary phases and maintains the elements solutionized in the matrix [30,31].

Subsequently, for both the conditions, the lattice parameter value decreased under thermal exposure, but more significantly for the SOL state. The compression stresses on the surface induced by the quenching after the solution treatment have been removed during the polishing of the SOL samples before the oxidation treatment. In fact, the chemical homogenization generated by the solution annealing leads to the formation of larger precipitates in the SOL state when subjected to heat treatment, producing a more remarkable chemical element depletion from the **γ**-phase, thus reducing more intensely the lattice parameters of **γ**-phase compared to the AB state.

It should be noted that the residual stresses generated during the fabrication process, as well as during the solution treatment followed by water quenching, can affect the value of lattice parameters. However, the high oxidation thermal exposure at 900 °C act as stress-relieving, since the thermal exposure is superior to the typical stress-relieving employed for this alloy (870 °C).

Therefore, the initial residual stresses are progressively mitigated during the thermal exposures at 900 °C. After thermal exposures for 96 h, the impact of the residual stresses induced by the AB condition and solutionizing (plus water quenching) can be considered negligible. At this stage, after 96 h, the SOL state still presents a lower lattice parameter than the AB one, analogous as the conditions under 8 h of thermal exposures. This indicates a more pronounced depletion of elements from the matrix and, therefore, more marked precipitation of phases than in the AB state. Hence, it is possible to infer that the high precipitation provoked internal stresses triggering the spalling of the oxides in the SOL state. The presence of local stresses due to the phases precipitation is reported in literature [50].

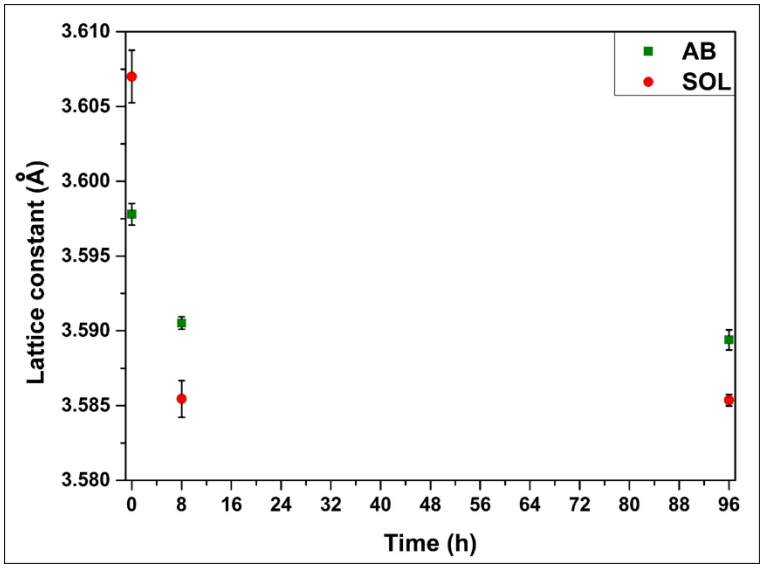

Figure 20: lattice constant evolution during oxidation treatment at 900 °C for the AB and SOL states

3.5 Scratch test analysis

Fig.21 summarizes the results of the scratch tests for the investigated conditions, reporting the lateral force value needed for the indenter lateral movement vs the normal force applied by the indenter for one parallel and one perpendicular scratch tests. In the graphs in Fig.21, it is possible to see that the later force value increases with the increment of the normal force, at first with a nearly linear behavior, then increasing in a more markedly way. The point where the linear behavior stops represent the first contact between the indenter and the alloy below the oxide layer. The normal force needed to reach the alloy has been evaluated for each scratch, and the results are reported in Table 3.

The AB condition after 8 h of oxidation shows just a minimal difference between the parallel and perpendicular tests, reaching lower normal force values for the latter. This can be correlated to the anisotropy of the grain characteristic for the AB samples. The SOL condition after 8 h of oxidation does not show any differences between the scratch test orientations because of the more equiaxed and isotropic grains structure [7,30,31].

After 96 h of oxidation, the sample in the AB condition does not show any significant differences between the two test orientations due to the increased thickness of the oxide layer. Furthermore, also the normal force required to reach the alloy raises because the oxide layer thickness is increased compared to the 8 h condition, reaching values of around 200 mN for both test orientations. However, the anisotropy of the grains is still visible (see in the SEM images in Fig.22e and Fig.22f). The SOL condition after 96 h of oxidation does not show any differences between the scratch test orientations because of the grains isotropy. Moreover, the oxide possesses a slightly lower resistance compared to the AB condition oxidized for 96 h, with normal force values below 190 mN. These slightly lower values may be caused by the presence of the mixed oxides or by the oxide defects. However, the force needed to reach the alloy is not so different between the AB and the SOL state, because, in both cases, the oxide layer is mainly composed of Cr_2O_3. The GBs are covered by the oxide also for this condition (Fig.22g and Fig.22h), showing the bigger grain size and isotropy of the SOL state in comparison to the AB state.

As it can be noticed in Fig.22, no cracks or big oxide removals are present after the scratch test, indicating that the general adhesion of the oxide is similar for all conditions. This similar mechanical behavior for the two conditions indicates that the defects formation in the SOL samples is not related to a different mechanical resistance between the two oxides. Therefore, the reason for the defect formation can be related to the coarser microstructure coupled with the local stress generated by more pronounced precipitation than the AB case, as determined by XRD analysis.

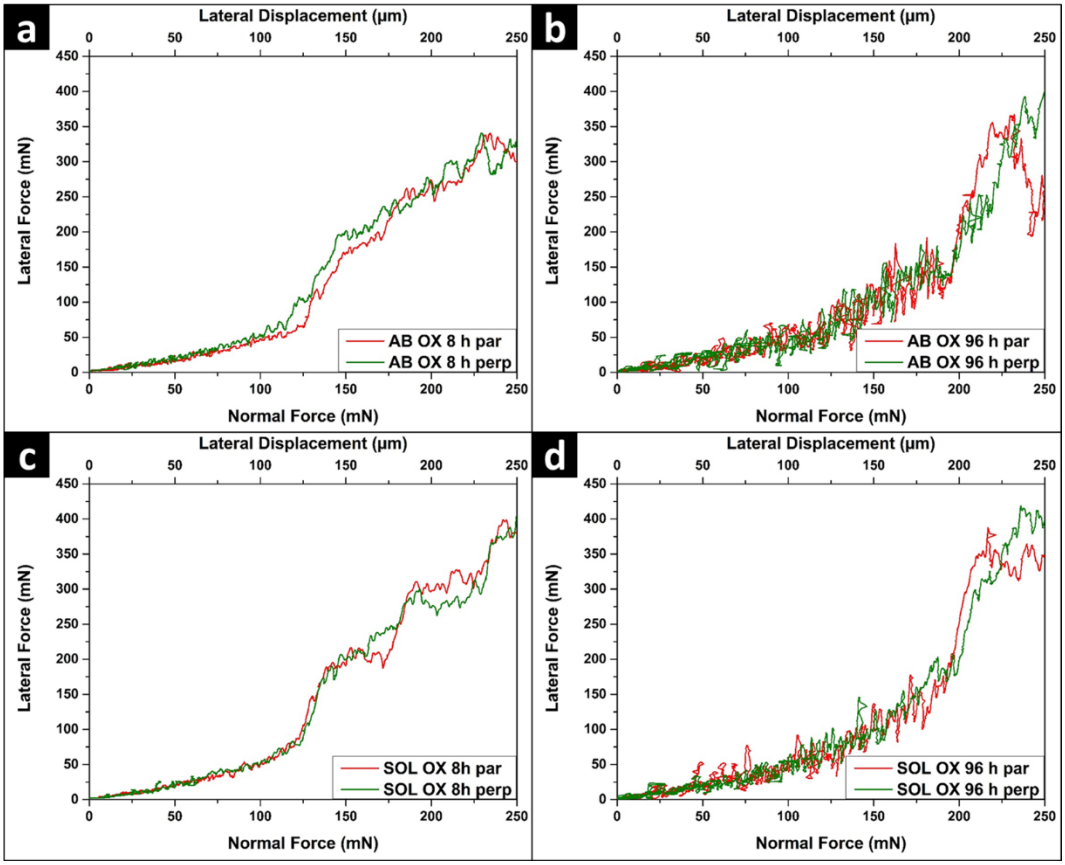

Figure 21: Lateral force versus normal force reported from scratch tests of AB 8 h (a), AB 96 h (b), SOL 8 h (c) and SOL 96 h (d)

Table 3: Normal force needed to reach the alloy

Average Normal Force of scratch:	**AB 8 h** Normal force (mN)	**SOL 8 h** Normal force (mN)	**AB 96 h** Normal force (mN)	**SOL 96 h** Normal force (mN)
Parallel	122±3	127±4	201±10	185±6
Perpendicular	115±2	125±5	202±14	188±10

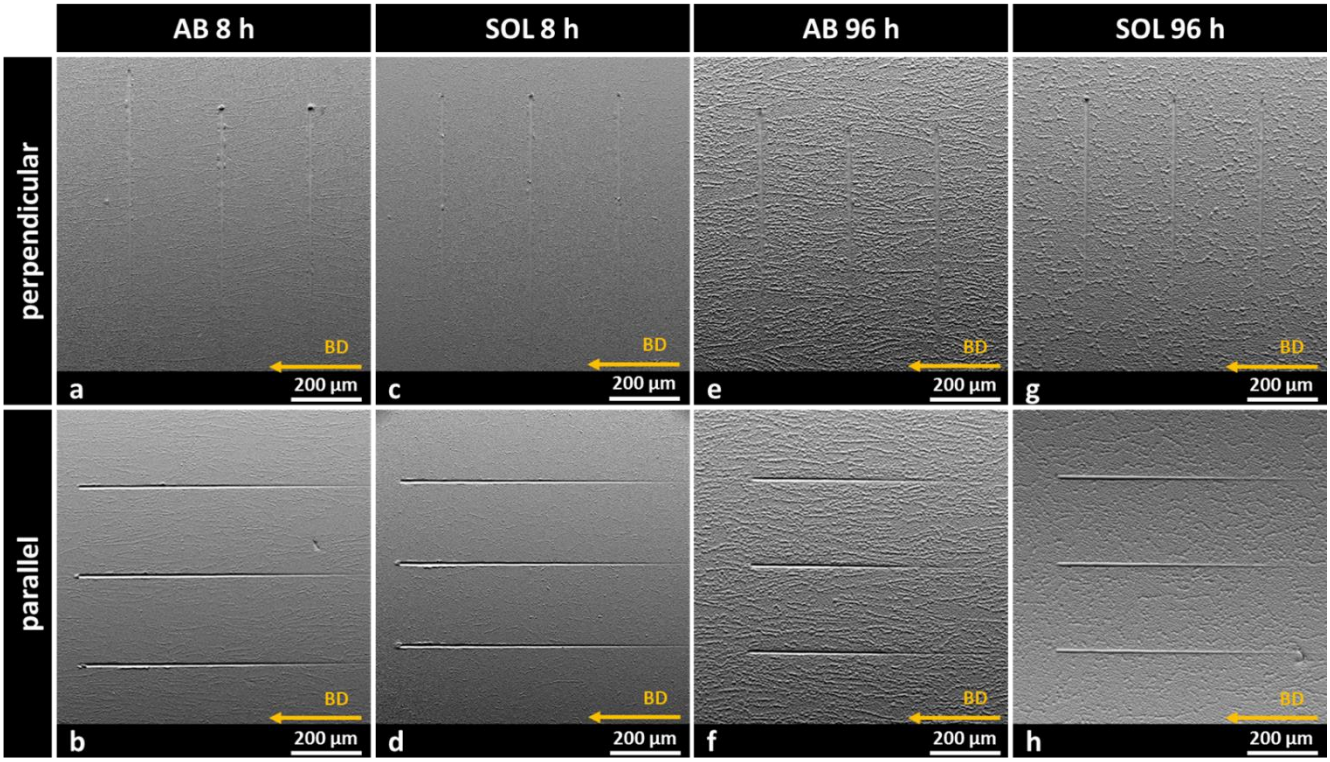

Figure 22: SEM images of scratch tests perpendicular to the BD of the AB 8 h (a), AB 96 h (e), SOL 8 h (c), SOL 96 h (g) and parallel to the BD of AB 8 h (b), AB 96 h (f), SOL 8 h (d) and SOL 96 h (h)

4.0 Conclusions

The paper summarizes the oxidation behavior of IN625 alloy fabricated by LPBF in the AB and solution annealed at 1150 °C for 2 h states under thermal exposures at 900 °C in air up to 96 h. The main conclusions are:

1. For both conditions, the oxide layer was mainly composed of Cr_2O_3. The oxide also showed the presence of TiO_2 after thermal exposures. For the SOL conditions, after thermal exposures at 900 °C for 96 h, also other oxides, such as $NiCr_2O_4$ and Nb_2O_5, were detected in the form of clusters located inside the Cr_2O_3 oxide layer;
2. AB possesses higher oxidation resistance compared to the SOL state, slowly reducing its oxidation rate during the time thanks to the formation of a compact oxide layer;
3. Local spalling in SOL samples caused reduced oxidation resistance, which can be attributed to the presence of coarser phases coupled with the local stress generated by more pronounced precipitation than the AB case, as determined by XRD analyses;
4. Scratch tests revealed that the mechanical resistance of the oxide was almost identical for both conditions. Cracks and spalling in SOL samples were localized on the outer oxide layer, revealing that the mixed oxides observed did not reduce the oxide layer properties.

Data availability

The authors declare that the main data supporting the findings of this work are available within the article.

Acknowledgments

The authors would like to acknowledge the Integrated Additive Manufacturing Centre at Politecnico di Torino (IAM@PoliTo) where the specimens were fabricated.

The part of this work at Chalmers has been performed in the framework of the Centre for Additive Manufacturing – Metal (CAM^2), supported by Swedish Governmental Agency of Innovation Systems (Vinnova).

References

[1] S. FLOREEN, G. FUCHS, W. YANG, the Metallurgy of Alloy-625, Superalloys. (1994) 13–37. doi:10.7449/1994/Superalloys_1994_13_37.

[2] L. Garcia-Fresnillo, A. Chyrkin, C. Böhme, J. Barnikel, F. Schmitz, W.J. Quadakkers, Oxidation behaviour and microstructural stability of alloy 625 during long-term exposure in steam, J. Mater. Sci. 49 (2014) 6127–6142. doi:10.1007/s10853-014-8344-7.

[3] M. Xia, D. Gu, C. Ma, H. Zhang, D. Dai, H. Chen, C. Li, Z. Zhou, G. Chen, I. Kelbassa, Fragmentation and refinement behavior and underlying thermodynamic mechanism of WC reinforcement during selective laser melting of Ni-based composites, J. Alloys Compd. 777 (2019) 693–702. doi:10.1016/j.jallcom.2018.11.056.

[4] C. Hong, D. Gu, D. Dai, M. Alkhayat, W. Urban, P. Yuan, S. Cao, A. Gasser, A. Weisheit, I. Kelbassa, M. Zhong, R. Poprawe, Laser additive manufacturing of ultrafine TiC particle reinforced Inconel 625 based composite parts: Tailored microstructures and enhanced performance, Mater. Sci. Eng. A. 635 (2015) 118–128. doi:10.1016/j.msea.2015.03.043.

[5] I.A. Choudhury, Machinability of nickel-base super alloys : a general review, J. Mater. Process. Technol. 77 (1998) 278–284.

[6] E.O. Ezugwu, Key improvements in the machining of difficult-to-cut aerospace superalloys, Int. J. Mach. Tools Manuf. 45 (2005) 1353–1367. doi:10.1016/j.ijmachtools.2005.02.003.

[7] G. Marchese, M. Lorusso, S. Parizia, E. Bassini, J.W. Lee, F. Calignano, D. Manfredi, M. Terner, H.U. Hong, D. Ugues, M. Lombardi, S. Biamino, Influence of heat treatments on microstructure evolution and mechanical properties of Inconel 625 processed by laser powder bed fusion, Mater. Sci. Eng. A. 729 (2018) 64–75. doi:10.1016/j.msea.2018.05.044.

[8] L.N. Carter, X. Wang, N. Read, R. Khan, M. Aristizabal, K. Essa, M.M. Attallah, Process optimisation of selective laser melting using energy density model for nickel based superalloys, Mater. Sci. Technol. 0836 (2016) 1–5. doi:10.1179/1743284715Y.0000000108.

[9] M. Xia, D. Gu, G. Yu, D. Dai, H. Chen, Q. Shi, Selective laser melting 3D printing of Ni-based superalloy: understanding thermodynamic mechanisms, Sci. Bull. 61 (2016) 1013–1022. doi:10.1007/s11434-016-1098-7.

[10] S.S. Babu, N. Raghavan, J. Raplee, S.J. Foster, C. Frederick, M. Haines, R. Dinwiddie, M.K. Kirka, A. Plotkowski, Y. Lee, R.R. Dehoff, Additive Manufacturing of Nickel Superalloys: Opportunities for Innovation and Challenges Related to Qualification, Metall. Mater. Trans. A Phys. Metall. Mater. Sci. 49 (2018) 3764–3780. doi:10.1007/s11661-018-4702-4.

[11] Z. Yan, W. Liu, Z. Tang, X. Liu, N. Zhang, M. Li, H. Zhang, Review on thermal analysis in laser-based additive manufacturing, Opt. Laser Technol. 106 (2018) 427–441. doi:10.1016/j.optlastec.2018.04.034.

[12] W. Zhang, A. De, A. Wilson-Heid, A.M. Beese, J.W. Elmer, J.S. Zuback, T. Mukherjee, J.O. Milewski, T. DebRoy, H.L. Wei, Additive manufacturing of metallic components – Process, structure and properties, Prog. Mater. Sci. 92 (2017) 112–224. doi:10.1016/j.pmatsci.2017.10.001.

[13] N. Li, S. Huang, G. Zhang, R. Qin, W. Liu, H. Xiong, G. Shi, J. Blackburn, Progress in additive manufacturing on new materials: A review, J. Mater. Sci. Technol. 35 (2019) 242–269. doi:10.1016/j.jmst.2018.09.002.

[14] A. Kreitcberg, V. Brailovski, S. Turenne, Elevated temperature mechanical behavior of IN625 alloy processed by laser powder-bed fusion, Mater. Sci. Eng. A. 700 (2017) 540–553. doi:10.1016/j.msea.2017.06.045.

[15] C. Li, R. White, X.Y. Fang, M. Weaver, Y.B. Guo, Microstructure Evolution Characteristics of Inconel 625 Alloy from Selective Laser Melting to Heat Treatment, Mater. Sci. Eng. A. (2017). doi:10.1016/j.msea.2017.08.058.

[16] G. Marchese, X. Garmendia Colera, F. Calignano, M. Lorusso, S. Biamino, P. Minetola, D. Manfredi, Characterization and Comparison of Inconel 625 Processed by Selective Laser Melting and Laser Metal Deposition, Adv. Eng. Mater. 19 (2017) 1–9. doi:10.1002/adem.201600635.

[17] D.M. Gorman, R.L. Higginson, H. Du, G. McColvin, A.T. Fry, R.C. Thomson, Microstructural analysis of IN617 and IN625 oxidised in the presence of steam for use in ultra-supercritical power plant, Oxid. Met. 79 (2013) 553–566. doi:10.1007/s11085-012-9342-2.

[18] M.Y. Xiao, Study on the Corrosion Behaviour of Nickel-Base Alloy 625 in Landfill Leachate Treated by Supercritical Water Oxidation, Adv. Mater. Res. 908 (2014) 93–97. doi:10.4028/www.scientific.net/AMR.908.93.

[19] K.H. Chang, S.M. Chen, T.K. Yeh, J.J. Kai, Effect of dissolved oxygen content on the oxide structure of Alloy 625 in supercritical water environments at 700°C, Corros. Sci. 81 (2014) 21–26. doi:10.1016/j.corsci.2013.11.034.

[20] H. Buscail, R. Rolland, C. Issartel, F. Rabaste, F. Riffard, L. Aranda, M. Vilasi, Effects of water vapour on the oxidation of a nickel-base 625 alloy between 900 and 1,100 °C, J. Mater. Sci. 46 (2011) 5903–5915. doi:10.1007/s10853-011-5544-2.

[21] E. N'dah, M.P. Hierro, K. Borrero, F.J. Pérez, Study of the cyclic oxidation resistance of superalloy IN-625: Lifetime predicted by COSP-modelling program, Oxid. Met. 68 (2007) 9–21. doi:10.1007/s11085-006-9048-4.

[22] Q. Jia, D. Gu, Selective laser melting additive manufactured Inconel 718 superalloy parts: High-temperature oxidation property and its mechanisms, Opt. Laser Technol. 62 (2014) 161–171. doi:10.1016/j.optlastec.2014.03.008.

[23] X. Wang, L.N. Carter, B. Pang, M.M. Attallah, M.H. Loretto, Microstructure and yield strength of SLM-fabricated CM247LC Ni-Superalloy, Acta Mater. 128 (2017) 87–95. doi:10.1016/j.actamat.2017.02.007.

[24] M.J. Donachie, S.J. Donachie, Superalloys A Technical Guide, 2002. doi:10.1361/stgs2002p001.

[25] N.H. Sateesh, G.C.M. Kumar, K. Prasad, S. C.K., A.R. Vinod, Microstructure and Mechanical Characterization of Laser Sintered Inconel-625 Superalloy, Procedia Mater. Sci. 5 (2014) 772–779. doi:10.1016/j.mspro.2014.07.327.

[26] J.N. Dupont, Solidification of an alloy 625 Weld Overlay, Metall. Mater. Trans. A Phys. Metall. Mater. Sci. 27 (1996) 3612–3620. doi:10.1007/BF02595452.

[27] G. Marchese, E. Bassini, M. Calandri, E.P. Ambrosio, F. Calignano, M. Lorusso, D. Manfredi, M. Pavese, S. Biamino, P. Fino, Microstructural investigation of as-fabricated and heat-treated Inconel 625 and Inconel 718 fabricated by direct metal laser sintering: contribution of Politecnico di Torino and Istituto Italiano di Tecnologia (IIT) di Torino, Met. Powder Rep. 71 (2016) 273–278. doi:10.1016/j.mprp.2016.06.002.

[28] S.M. Corporation, Inconel Alloy 625, Www.Specialmetals.Com. 625 (2013) 1–28. doi:SMC-066.

[29] H. Chandler, Heat Treater ' s Guide: Practices and Procedures for Nonferrous Alloys, 1996.

[30] A. Kreitcberg, V. Brailovski, S. Turenne, Effect of heat treatment and hot isostatic pressing on the microstructure and mechanical properties of Inconel 625 alloy processed by laser powder bed fusion, Mater. Sci. Eng. A. 689 (2017) 1–10. doi:10.1016/j.msea.2017.02.038.

[31] G. Marchese, S. Parizia, M. Rashidi, A. Saboori, D. Manfredi, D. Ugues, M. Lombardi, E. Hryha, S. Biamino, The role of texturing and microstructure evolution on the tensile behavior of heat-treated Inconel 625 produced via laser powder bed fusion, Mater. Sci. Eng. A. 769 (2019) 138500. doi:10.1016/j.msea.2019.138500.

[32] M. Cabrini, S. Lorenzi, C. Testa, T. Pastore, F. Brevi, S. Biamino, P. Fino, D. Manfredi, G. Marchese, F. Calignano, F. Scenini, Evaluation of Corrosion Resistance of Alloy 625 Obtained by Laser Powder Bed Fusion, J. Electrochem. Soc. 166 (2019) C3399–C3408. doi:10.1149/2.0471911jes.

[33] M. Cabrini, S. Lorenzi, C. Testa, F. Brevi, S. Biamino, P. Fino, D. Manfredi, G. Marchese, F. Calignano, T. Pastore, Microstructure and selective corrosion of alloy 625 obtained by means of laser powder bed fusion, Materials (Basel). 12 (2019) 1–11. doi:10.3390/ma12111742.

[34] N. Ramenatte, A. Vernouillet, S. Mathieu, A. Vande Put, M. Vilasi, D. Monceau, A comparison of the high-temperature oxidation behaviour of conventional wrought and laser beam melted Inconel 625, Corros. Sci. 164 (2020) 108347. doi:10.1016/j.corsci.2019.108347.

[35] L. Chen, Y. Sun, L. Li, X. Ren, Effect of heat treatment on the microstructure and high temperature oxidation behavior of TiC/Inconel 625 nanocomposites fabricated by selective laser melting, Corros. Sci. 169 (2020) 108606. doi:10.1016/j.corsci.2020.108606.

[36] S. Pedrazzini, E.S. Kiseeva, R. Escoube, H.M. Gardner, J.O. Douglas, A. Radecka, P.M. Mignanelli, G.M. Hughes, G. Chapman, P.D. Edmondson, H.J. Stone, D. De Lille, P.A.J. Bagot, In-Service Oxidation and Microstructural Evolution of a Nickel Superalloy in a Formula 1 Car Exhaust, Oxid. Met. 89 (2018) 375–394. doi:10.1007/s11085-017-9792-7.

[37] R. Buck, S. Giuliano, R. Uhlig, Central tower systems using the brayton cycle, Elsevier Ltd, 2017. doi:10.1016/B978-0-08-100516-3.00016-2.

[38] J.B. Nelson, D.P. Riley, An experimental investigation of extrapolation methods in the derivation of accurate unit-cell dimensions of crystals, Proc. Phys. Soc. 57 (1945) 160–177. doi:10.1088/0959-5309/57/3/302.

[39] G.P. Dinda, A.K. Dasgupta, J. Mazumder, Laser aided direct metal deposition of Inconel 625 superalloy: Microstructural evolution and thermal stability, Mater. Sci. Eng. A. 509 (2009) 98–104. doi:10.1016/j.msea.2009.01.009.

[40] M. Calandri, D. Manfredi, F. Calignano, E.P. Ambrosio, S. Biamino, R. Lupoi, D. Ugues, Solution Treatment Study of Inconel 718 Produced by SLM Additive Technique in View of the Oxidation Resistance, Adv. Eng. Mater. (2018) 1–16. doi:10.1002/adem.201800351.

[41] H.A. Miley, THEORY OF OXIDATION AND TARNISHING OF METALS. I. The linear, parabolic and logarith, J. Electrochem. Soc. 81 (1942) 391–411.

[42] L. Kumar, R. Venkataramani, M. Sundararaman, P. Mukhopadhyay, S.P. Garg, Studies on the oxidation behavior of inconel 625 between 873 and 1523 K, Oxid. Met. 45 (1996) 221–244. doi:10.1007/BF01046827.

[43] A. Chyrkin, P. Huczkowski, V. Shemet, L. Singheiser, W.J. Quadakkers, Predicting subsurface

enrichment/depletion processes during high-temperature oxidation of alloy 625 thin foils, 18th Int. Corros. Congr. 2011. 2 (2011) 1–11.

[44] A. Chyrkin, P. Huczkowski, V. Shemet, L. Singheiser, W.J. Quadakkers, Sub-scale depletion and enrichment processes during high temperature oxidation of the nickel base alloy 625 in the temperature range 900-1000 °c, Oxid. Met. 75 (2011) 143–166. doi:10.1007/s11085-010-9225-3.

[45] M. Pröbstle, S. Neumeier, J. Hopfenmüller, L.P. Freund, T. Niendorf, D. Schwarze, M. Göken, Superior creep strength of a nickel-based superalloy produced by selective laser melting, Mater. Sci. Eng. A. 674 (2016) 299–307. doi:10.1016/j.msea.2016.07.061.

[46] E.A. Lass, M.R. Stoudt, M.B. Katz, M.E. Williams, Precipitation and dissolution of δ and γ" during heat treatment of a laser powder-bed fusion produced Ni-based superalloy, Scr. Mater. 154 (2018) 83–86. doi:10.1016/j.scriptamat.2018.05.025.

[47] S.D.K. John N.DuPont, John C. Lippold, Welding Metallurgy and Weldability of Nickel-base Alloys, 2009.

[48] F. Zhang, L.E. Levine, A.J. Allen, M.R. Stoudt, G. Lindwall, E.A. Lass, M.E. Williams, Y. Idell, C.E. Campbell, Effect of heat treatment on the microstructural evolution of a nickel-based superalloy additive-manufactured by laser powder bed fusion, Acta Mater. 152 (2018) 200–214. doi:10.1016/j.actamat.2018.03.017.

[49] M.R. Stoudt, E.A. Lass, D.S. Ng, M.E. Williams, F. Zhang, C.E. Campbell, G. Lindwall, L.E. Levine, The Influence of Annealing Temperature and Time on the Formation of δ-Phase in Additively-Manufactured Inconel 625, Metall. Mater. Trans. A Phys. Metall. Mater. Sci. 49 (2018) 3028–3037. doi:10.1007/s11661-018-4643-y.

[50] L.N. Carter, M.M. Attallah, R.C. Reed, Laser Powder Bed Fabrication of Nickel-Base Superalloys: Influence of Parameters; Characterisation, Quantification and Mitigation of Cracking, Superalloys 2012. (2012) 577–586. doi:10.1002/9781118516430.ch64.